Title
Simultaneous Operando Measurements of the Local Temperature, State of Charge, and Strain inside a Commercial Lithium-Ion Battery Pouch Cell

Journal
Journal of The Electrochemical Society, 165(7)

ISSN
0013-4651

Authors
Yu, Xinghua
Feng, Zhili
Ren, Yang
et al.

Publication Date
2018

DOI
10.1149/2.1251807jes

Peer reviewed

Simultaneous Operando Measurements of the Local Temperature, State of Charge, and Strain inside a Commercial Lithium-Ion Battery Pouch Cell

Xinghua Yu,[1] Zhili Feng,[1,z] Yang Ren,[2] Daniel Henn,[3] Zhenggang Wu,[1] Ke An,[4] Bi Wu,[5] Christian Fau,[5] Chen Li,[6] and Stephen J. Harris[7,*]

[1]*Materials Science and Technology Division, Oak Ridge National Laboratory, Oak Ridge, Tennessee 37831, USA*
[2]*X-ray Science Division, Advanced Photon Source, Argonne National Laboratory, Lemont, Illinois 60439, USA*
[3]*Department of Chemistry, University of Tennessee, Knoxville, Tennessee 37996, USA*
[4]*Spallation Neutron Source, Oak Ridge National Laboratory, Oak Ridge, Tennessee 37831,USA*
[5]*Formally with Honda R&D Americas, Inc, Ann Arbor, Michigan 48109, USA*
[6]*ZeeAero, Mountain View, California 94043, USA*
[7]*Materials Science Division, Lawrence Berkeley National Lab, Berkeley, California 94720, USA*

A high energy X-ray diffraction technique is employed in a new way to make operando through-thickness measurements inside a large format commercial Li-ion pouch cell. The technique, which has a sub-mm in-plane spatial resolution, simultaneously determines the local temperature, the local state of charge of both electrodes (as opposed to the global average state of charge determined electrochemically), and the local in-plane elastic strain in the current collectors, all without embedding any intrusive sensors that alter battery behavior. As both thermal strain and mechanical strain develop during the charge-discharge cycling of the pouch cell, a novel approach developed herein makes it possible to separate them, allowing for measurement of the local temperature inside the battery. The operando experiment reveals that the temperature inside the cell is substantially higher than the external temperature. We propose that mechanical strain is due primarily to load transfer from the electrode to the current collector during lithiation, allowing determination of the local binder. Detailed local SOC mapping illustrates non-uniform degradation of the battery pouch cell. The possibility for 3D measurements is proposed. We believe that this new approach can provide critically needed data for validation of detailed models of processes inside commercial pouch cells.
 [DOI: 10.1149/2.1251807jes]

Manuscript submitted February 9, 2018; revised manuscript received April 23, 2018. Published May 23, 2018.

Today's electric vehicles generally use pouch cells rather than the more traditional cylindrical cells. An important advantage of pouch cells is their much higher surface-to-volume ratio for a given capacity, which permits better cooling. Batteries tend to heat up because of the hot environments that cars experience, internal electric resistance heating, and exothermic chemical reactions during operation. The performance of batteries fades over time, and high temperatures (say, above 45°C) greatly accelerate the fade rate[1,2] and may promote thermal runaway,[3] making temperature control critical.[4,5] Ideally, temperature control should be guided by the temperature inside the pouch cell, but making measurements inside an operating pouch cell has been difficult. Instead, the outside temperature has usually been taken as a surrogate for the internal temperature.[6–8]

If pouch cells are sufficiently thin, and if the thermal conductivity is high enough, then it is reasonable to assume that the temperature measured at an *x-y* location on the outside of a pouch cell, with a thermocouple or with a thermal infrared (IR) camera, is close to the temperature at that *x-y* location all the way through its thickness.[9] However, auto makers are motivated to make pouch cells thicker, reducing the number of expensive seals, electrical connections, and controls. Since local temperatures inside a thick cell might well be too high under some conditions, knowledge of the spatial distribution of internal temperature is of vital importance for achieving long life at low cost.

A number of techniques have been developed to measure internal cell temperatures,[10–17] but measurement of local temperatures for unaltered commercial (thick) cells can be challenging. The temperature can also be estimated using electrical-thermal models,[2,9,18–22] but they require accurate internal temperature data and thermal constants for validation and calibration. In this paper we describe a novel method for making line-of-sight operando internal measurements maps that simultaneously provide local temperature, local state of charge (SOC), and local mechanical strain inside a large format Li-ion pouch cell by using high energy X-ray diffraction (HE-XRD) to monitor the lattice spacing changes in the electrodes and in the current collectors. Nominal in-plane spatial resolution is 0.3 mm, permitting observation of spatial variations or heterogeneities[8,23–25] of properties involved in performance and fade. This work follows our previous studies using neutron diffraction in which we made 2D time-dependent SOC maps demonstrating that failure in our pouch cell was strongly heterogeneous;[24,26,27] and the work of Paxton et al.,[28] using X-rays, who also observed heterogeneities in cells. The present work also clarifies the role of mechanically induced strain,[29,30] which has been ignored in some recent diffraction studies of internal temperatures carried out with both neutron and X-ray sources.[31–35] We believe that extending the technique to 3D may be possible with further development of the measurement technique.[36] Monitoring the time evolution of these 2D and 3D maps will allow us to determine local internal thermal conductivities[37–39] as well as time-dependent heat transfer rates from the pouch interior to the environment.[40]

Experimental

A commercial 4.7 Ah pouch cell with dimensions 140 × 102 × 14 mm was used in this study. The battery materials were enclosed in a rigid aluminum casing. The cathode was $Li_xNi_yMn_zCo_{(1-y-z)}O_2$ (NMC). The space group of the crystal structure is R-3m (#166). The lattice parameters vary a bit with the exact composition, but for NMC-333 we have $a = b = 2.86$ angstroms and $c = 14.227$ angstroms. The transition metal is in 3a sites, Li is in 3b, and O is in 6c. The carbon anode was apparently amorphous, based on our inability to see a diffraction signature. The high-energy X-ray diffraction (HE-XRD) study was carried out at the 11-ID-C beam line at the Advanced Photon Source, Argonne National Laboratory. A Si (311) single crystal monochromator was used to provide a 105.7 keV X-ray ($\lambda = 0.1173$ Å) with beam size of 0.3 mm × 0.3 mm that is incident perpendicular to the plane of the pouch. Since properties may vary though the pouch thickness, we refer to our measurements as line-of-sight averaged. Absorption of these high energy X-rays is

*Electrochemical Society Member.
[z]E-mail: fengz@ornl.gov

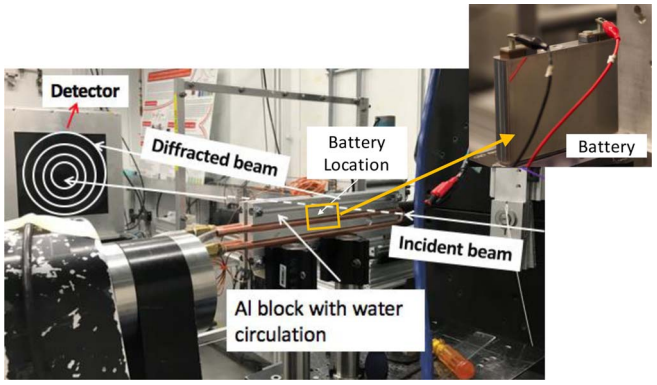

Figure 1. Operando synchrotron experimental setup, with insert showing the battery before sandwitched between two aluminum blocks for temperature control.

low, allowing XRD measurements to be made through thick cells and minimizing any damage to the electrode materials.

The experimental setup is shown in Figure 1. The plane of the battery (the *x-y* plane) was perpendicular to the X-ray beam. The incident beam passed through the 14-mm thick cell and was detected with a large area pixel detector placed on the 2-theta axis. Diffraction rings were recorded by the pixel detector and analyzed. An automated *x-y* translation stage was used to position the battery relative to the X-ray beam line for ex-situ 2D mapping of spatial variation/heterogeneity of battery properties. For the present operando measurements, the beam line passed through the center of the cell.

Changes in lattice spacing (*d*-spacing) of crystalline electrode materials (cathode, anode, and current collectors)[30] during charging and discharging of a lithium ion battery stem from volumetric changes due to lithiation;[41–43] thermal expansion;[44] and stress/mechanical deformation,[30,45,46] for example, if particles impinge on one another,

$$\Delta d = \Delta d^{chem} + \Delta d^{therm} + \Delta d^{mech} \quad [1]$$

where Δd is the total lattice space change, measured by the HE-XRD, of an electrode or current collector material as the cell is being charged/discharged. Since neither the aluminum nor the copper current collectors are lithiated during normal cell operation, we have[40]

$$\Delta d_{cc} = \Delta d^{therm} + \Delta d^{mech} \quad [2]$$

The total strain, ε, from the lattice spacing measurement results can be calculated as:

$$\varepsilon = \frac{\Delta d}{d^0} = \frac{\mathrm{d} - d^0}{d^0} \quad [3]$$

where d is the measured lattice spacing at given state of charge and temperature, and d^0 is the lattice spacing at a reference state.

In the present work, a set of experiments was devised to separate thermal and mechanical strain in the current collector by monitoring XRD spectra during charging at constant temperature in one set of experiments, and during heating at constant SOC in a second set of experiments.

In the constant temperature experiments, the temperature was controlled with a pair of aluminum heat sinks clamped to the cell. Water at the desired temperatures was circulated to control the heat sink temperature, and the battery was charged at a relatively slow charging rate of 0.25C at three different temperatures: 10°C, 25°C, and 40°C. Time resolved XRD data was taken with a 5 second exposure time. Since the thermal strain is unchanged in these constant temperature experiments, the change in the current collector lattice spacing gives the mechanical strain due to lithiation at the fixed internal temperature T

$$\varepsilon^{e}_{ccT} = \frac{\Delta \mathrm{d}_T}{d^0_T} = \frac{d_T - d^0_T}{d^0_T} \quad [4]$$

where d_T and $d^0{}_T$ are the measured lattice spacings of the current collector at the same temperature. (We show below that the mechanical strain is always in the elastic regime in our study.)

For the constant SOC experiments, we heated the cell from 10°C to 25°C and then from 25°C to 40°C, at 100% SOC, with a slow heating rate of approximately 1°C/min to help ensure that the internal temperature was relatively uniform. The results from such experiments were used to determine the effective thermal expansion coefficients of current collectors and electrode materials, which can be used to simultaneously measure the operando local temperature, elastic strain, and local SOC inside our large format commercial pouch cell. In our experiment, the thermal expansion coefficient was determined by regression analysis, to obtain an averaged value over the temperature range of interest.

$$\alpha_{cc} = \frac{d_{cc} - d^0_{cc}}{T - T^0} \quad [5]$$

During typical battery operation, both temperature and SOC may change. The elastic mechanical strain in the current collector, $\varepsilon^{e}{}_{cc,}$ is given in the following more general form:

$$\varepsilon^{mech}_{cc} = \frac{\Delta \mathrm{d}^{mech}_{cc}}{\Delta d^0_{cc}} = \frac{\Delta \mathrm{d}_{cc} - \Delta \mathrm{d}^{therm}_{cc}}{\Delta d^0_{cc}} = \frac{d_{cc} - d^0_{cc}}{d^0_{cc}} - \alpha_{cc}\left(T - T^0\right) \quad [6]$$

T^{o} and $d^{\circ}{}_{cc}$ are the internal temperature and lattice spacing at a reference state, for example, at 25°C and 0% of SOC.

We hypothesize that the origin of most of the mechanical strain in the current collector is load transfer from the adjacent electrode, which is strained as it lithiates.[30,42] Other factors contributing to the mechanical strain in the current collector could include thermal expansion mismatch between current collector and electrode, internal pressure buildup during operation and aging of the battery, and external stresses from battery packaging. We note that in our experimental setup, we measure the line-of-sight average strain in the plane of the current collector, which is perpendicular to the direction of the X-ray beam.

Finally, in the last set of experiments, we charged the cell at 2C and 20C without the heat sink, so that the surface of the battery was exposed to free air convection. Under such relatively fast charging rates, especially at the 20C charging rate, the internal temperature can be expected to rise. The HE-XRD exposure time was 1 s for the 2C tests and 0.2 s for the 20C tests. The (external) surface temperature of the battery was recorded with a Type-K thermocouple in the 20C test. For the 20C charging rate, an infrared thermal imaging camera was also used to record the surface temperature distribution as function of charging time. The battery surface was painted black to have uniform emissivity to ease the conversion of measured infrared intensity to temperature. Results from the above constant temperature and constant SOC experiments were used to determine simultaneously the changes in temperature and mechanical strain of the battery under relatively fast operando conditions.

In addition to the above operando measurements, we also conducted 2D ex-situ mapping experiments to determine local SOC fade of the battery after degradation. Figure 2 shows the locations of the local SOC measurements. A total of 1785 locations on a 51 by 35 grid were measured. The spacing between the measurement locations was 2 mm, with beam size of 0.3 mm.

Diffraction data were analyzed by Rietveld refinement with the GSAS (General Structure Analysis System) software.

Results

An X-ray diffraction spectrum of the cell in the fully discharged condition is shown Figure 3a. Multiple diffraction peaks were observed. These peaks were fitted with known diffraction peaks of the battery materials. Three phases were identified, the NMC cathode, Al from the case and the positive current collector, and the Cu negative current collector. Graphite peaks were not identified in the profile,

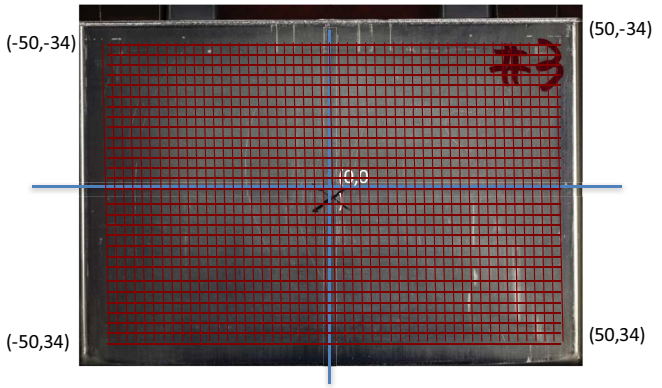

Figure 2. Locations of 2D Mapping of local SOC of the commercial battery. The coordinates of the four corners of mapping are shown in mm.

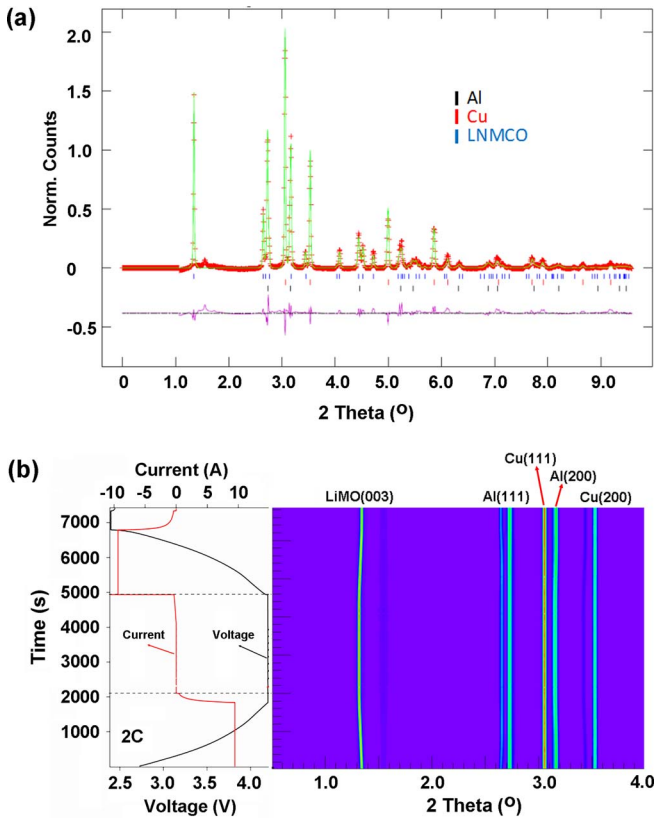

Figure 3. (a) X-ray diffraction (XRD) profile of the battery at fully discharged condition (2.4V) (b) The contour plot of the XRD profiles as a function of time during 2C cycling. The voltage and current are plotted in the side panel to the left of the diffraction data.

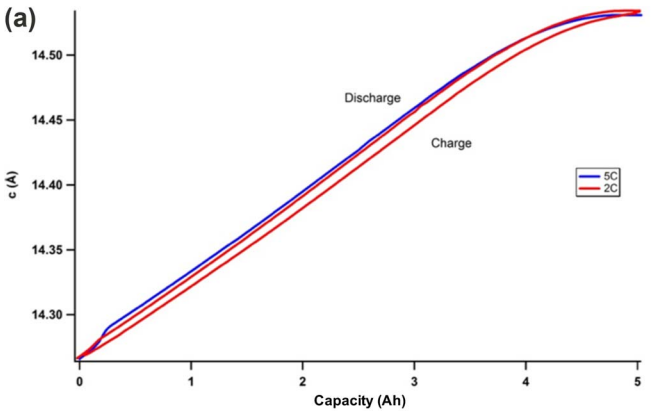

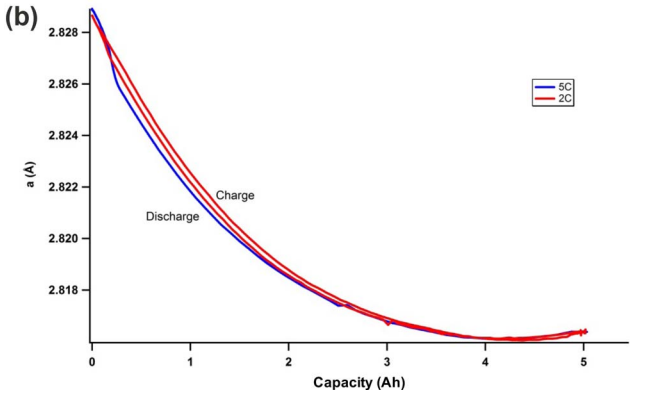

Figure 4. (a) correlation between the lattice spacing in c-direction [003] of cathode and SOC; (b) between the lattice spacing in a-direction and SOC. Charge and discharge at 2C, discharge at 5C.

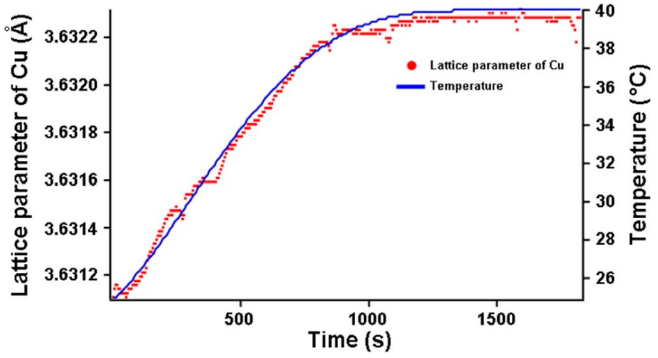

Figure 5. Cu lattice parameter vs. time when the battery was heated from 25°C to 40°C (SOC = 100%).

which suggests that the carbon anode material was amorphous. (The weak feature at $2\theta \sim 1.5$ degrees is thought to come from electrolyte or additives in the cell, as it did not change during cycling.) We note that, no Li peaks (neither HPC nor BCC) were observed after all three charging/discharging rates. Operando X-ray diffraction profiles collected during cycling at 2C are shown in Figure 3b. No new phases were observed during cycling.

As shown in Figure 3b, 2θ for the (003) line of the NMC cathode material in a fresh cell decreases during charging, indicating an increase of lattice parameter c, in agreement with the reported lattice parameter change for NMC.[47] Figure 4 shows the changes in lattice parameters c and a as functions of SOC (measured by coulomb counting and assuming that the SOC is uniform in this fresh cell) for charging and discharging at 2C and 5C and at 25°C. The relative change in lattice parameter c is about 5 times larger than that of a when the battery is charged from 0 to 100% SOC (2% vs 0.4%). Furthermore, for lattice parameter c, but not for a, there is a relatively linear and monotonic relationship between the lattice parameter and SOC. Thus, the local lattice parameter c can be used to determine the local SOC. The charging rate has almost no influence on these curves. Peak shifts in Cu and Al were also observed. The pouch cell had an Al casing, and we could not separate signals due to the Al casing from signals due to the Al current collectors. Therefore, we used the Cu lattice parameter changes to determine the internal temperature and mechanical stresses.

Figure 5 shows that the lattice parameter change correlates with the imposed temperature change during constant SOC heating (1°C/min heating rate). Regression curve fitting with Eq. 5 determined an effective thermal expansion coefficient for the Cu current collector of

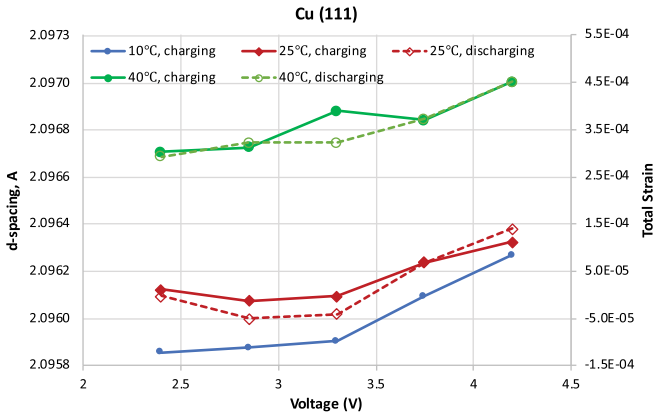

Figure 6. Results of the constant temperature charging/discharging test. Lattice spacing of Cu-(111) and total lattice strain as function of voltage. References for total strain calculation were 20C and 0% SOC.

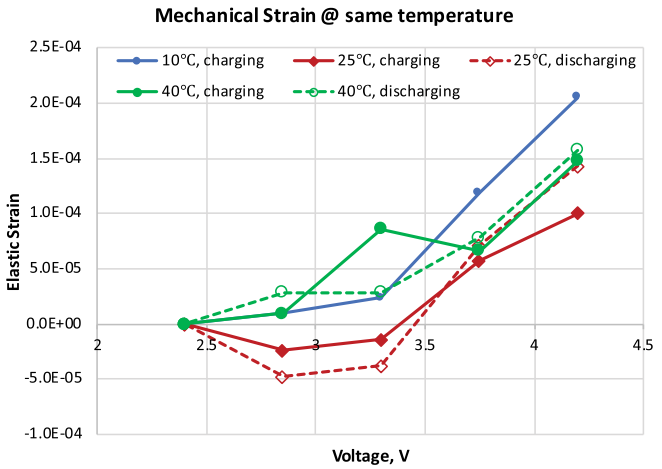

Figure 7. Isothermal elastic strain changes as function of SOC in 10C, 25C and 40C constant temperature tests. The reference state for strain calculation is 2.4V.

about $\alpha = 22 \times 10^{-6}$ K^{-1}, in reasonable agreement with the literature value of 17×10^{-6} K^{-1}. Similarly, we estimated α for the cathode material to be 40×10^{-6} K^{-1}. We note that to the extent that there is a large mismatch in thermal expansion coefficients between the current collectors and the composite electrode, there will be cyclic thermal stresses[48] that could lead to degradation of batteries from temperature excursions, for example from binder fatigue failure.[49]

Figure 6 presents the measured lattice spacing change and the total strain of the Cu current collector during constant temperature charging/discharging tests for three different temperatures, 10°C, 25°C, and 40°C. The reference temperature and SOC for total strain calculation were 25°C and 0% (2.4V) respectively. The left axis shows the lattice spacing change of Cu (111), while the right axis shows changes of the total lattice strain calculated with Eq. 3. It is evident that both temperature and SOC, as determined from the voltage, have strong influences on the lattice spacing and total strain, which includes both temperature strain and elastic mechanical strain, in the Cu current collector.

Figure 7 compares the isothermal cyclic changes in the elastic mechanical lattice strain in the Cu current collector due to battery charging/discharging, for three different constant temperature tests. The changes in elastic mechanical strain were calculated using Eq. 4. We note that, since the tests are isothermal, temperature-induced mechanical strain from thermal expansion mismatch is excluded. This makes it possible to examine the influence of SOC on the elastic mechanical strain only. Coincidentally, both thermal and mechanical strain are on the order of 10^{-4}. We note that the modulus of copper is about 50 times greater than the modulus of PVDF.

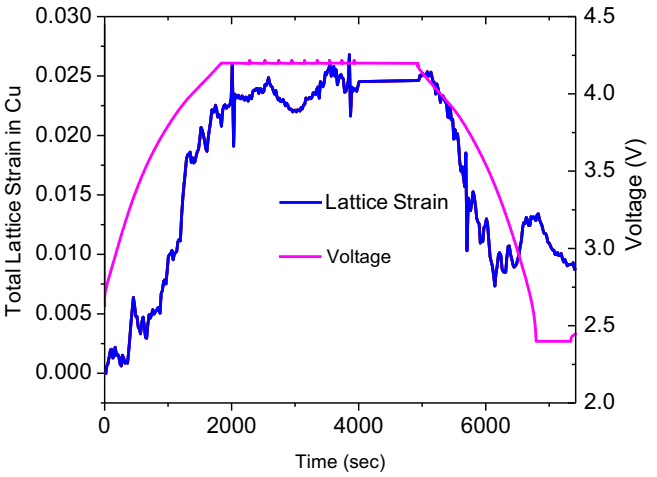

Figure 8. Total lattice strain in Cu current collector during 2C charging and discharging experiment.

As shown in the figure, the elastic strains at all three temperatures generally increase as a function of SOC, but the effects of temperature are weak, to within the strain measurement uncertainties (on the order of 10^{-5}). Therefore, we will assume, as a first order of approximation, that the correlation between the isothermal elastic mechanical strain and SOC is independent of temperature in our study. This can simplify the analysis of temperature and mechanical strains under more general battery operating conditions where both temperature and SOC changes during charging and discharging. We also see a modest and reversible change in strain in the current collector as we charge and discharge the cell. We note here that the measured strains are all small enough to be well within the elastic regime (i.e., below about 2×10^{-3}). It is likely that the presence of the soft separator substantially reduces any load transfer from the positive electrode to the Cu current collector. Therefore, we assign the mechanical lattice strain in the current collector primarily to elastic load transfer from the carbon/PVDF electrode as it lithiates and delithiates.

Figure 8 shows the evolution of the total lattice strain of the Cu current collector as a function of time during a 2C charge and discharge. During charge, both thermal and mechanical strains are positive, and we measure a combined strain of about 2.5×10^{-4}. During discharge, the thermal strain is again positive (the cell continues to get hotter), but the mechanical strain is negative as the negative electrode delithiates. Since we observe that the strain falls during discharge, mechanical strain dominates. We note, however, that even though the mechanical strain is completely reversed at the end of the full cycle, Figure 7, the total lattice strain ends up positive, at about 8×10^{-5}. We assign this "residual" strain to a temperature rise of $\varepsilon/\alpha \approx 3.5$°C.

In order to test this logic, we repeat the experiment at 20C, as shown in Figure 9a. Again, during charge, both thermal and mechanical strains are positive, leading to the combined strain of 3.9×10^{-4} shown in Figure 9b. During discharge, the thermal strain is again positive but the mechanical strain is negative. However, at 20C, where the temperature rise is greater than it was at 2C, the thermal and the mechanical strain are comparable, so the total strain is approximately constant during discharge. Since the mechanical strain has been reversed at discharge, the residual thermal strain is 3.9×10^{-4}, corresponding to a temperature rise at the end of the cycle of around 18°C.

Further analysis is possible for the 20C case, where we also have the external cell temperature (from a thermocouple) during charge and discharge, Figure 9a. As expected, the external temperature change is smaller than the 18°C internal temperature rise. Approximately 45% of the external temperature rise occurs during charge and about 55% during discharge. (Less electrical energy is available during discharge than was used during charge.) Delacourt et al. have shown that the

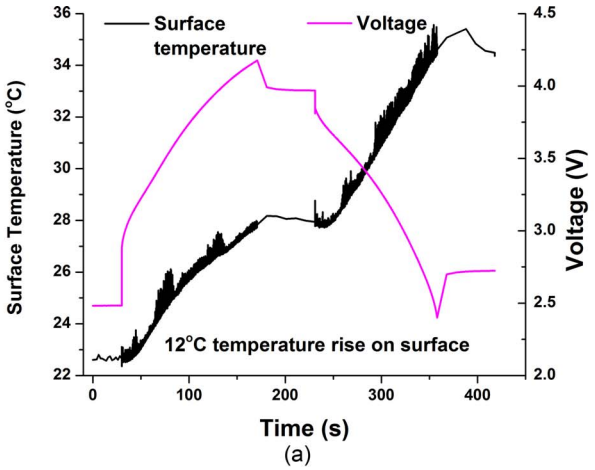

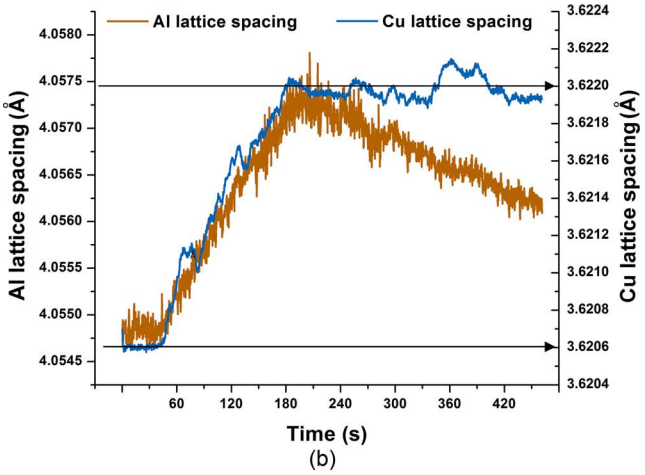

Figure 9. (a) Surface temperature and SOC and (b) Cu and Al current collector lattice spacing evolution in 20C charging/discharging experiment.

internal temperature rise is proportional to the external temperature rise.[17] This result implies that the internal temperature rise at the end of the charging step was about 8°C (0.45 × 18), corresponding to a thermal strain of 1.8×10^{-4}. Since the total strain at the end of charge was 3.9×10^{-4}, we estimate a mechanical strain during charge of 2.1×10^{-4}. More speculatively, if the temperature rise during 2C charge is again 45% of the ultimate temperature rise, we obtain, following the same logic, a thermal strain at the end of a 2C charge of 0.4×10^{-4}, (< 2°C) implying a mechanical strain during charge of 2.1×10^{-4}. Such close agreement between the estimated mechanical strains at 2C and 20C is fortuitous, suggests that mechanical strain is approximately independent of charging rate. (Figure 7 indicates that it is also approximately independent of temperature.). A combination of additional measurements and detailed modeling will be required to test these approximate calculations, but if the mechanical strain is generally insensitive to charging rate, separating strain and temperature will be much easier.

Discussion

Mechanical stresses.—Most electrode active materials change their volume upon lithiation,[43,50] and this can lead to stress buildup in pouch cells.[29,30] We hypothesize that the mechanical stresses that we observed in the Cu current collector were due primarily to load transfer from the expanding carbon electrode as it lithiated and, potentially, to thermal expansion mismatch in the 20C experiment. Graphite particles, expand by around 10% upon lithiation,[51] but that doesn't tell us how much a porous composite electrode expands.[42] Without some knowledge of the properties of the carbon, its microstructure, and the binder in our pouch cell, we cannot confirm this hypothesis.[52–54]

We suggest using mechanical strain in the current collectors to make semi-quantitative operando estimates for the evolution of local electrode-current collector adhesion. In pouch cells compressive forces holding electrodes together can be low, so a debonded electrode might well be in poor electrical contact with the current collector, reducing capacity.[29] We should be able to identify when and where this important failure mechanism occurs.[55,56] We have previously demonstrated heterogeneity in debonding in a graphite electrode using a simple ex-situ optical method, as seen in Figure 1 of Reference 26.[26] Furthermore, we speculate that an underlying cause of delamination can be the large thermal expansion coefficient mismatch[48] between the current collectors and the electrode material. This mismatch will induce mechanical stresses that may lead to fatigue failure in the binder for cells that undergo large temperature excursions. We will explore this hypothesis, of a relationship between local debonding and local temperature range, in future work.

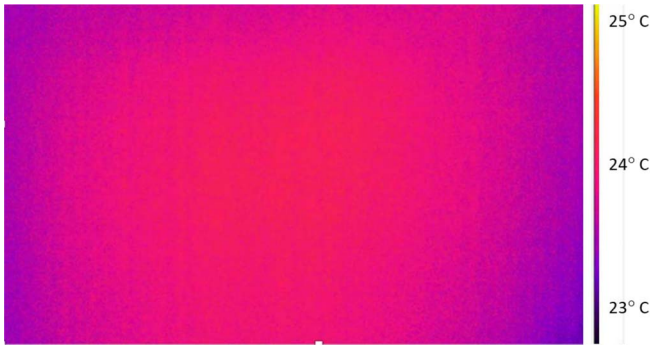

Figure 10. Surface temperature distribution measured by Infrared camera at 5% SOC at 20C charging rate.

2D maps of heterogeneous SOC.—In traditional macro-homogeneous battery models,[57] battery electrodes and particles are analyzed as 1D, homogeneous, and isotropic. While these models do an excellent job in accounting for battery performance, we have argued that such models do not in general capture detailed failure mechanisms.[24,27,58–63] The reason is that, like all materials, battery failure initiates at weak points and heterogeneities, which by definition don't exist in macro-homogeneous models. Thus, any detailed failure analysis can benefit from spatial maps, in 2D or—ideally—in 3D,[43,62,64] that provide the location, properties, and intensity of these weak points. For example, we believe that cell-to-cell variability of these heterogeneities can explain why the durability of nominally identical commercial cells is so variable.[65–67]

Figure 10 shows a surface temperature distribution measured by an infrared camera when the cell was exposed to air and was charged to 5% SOC at a 20C charging rate. The external temperature at the center of the battery is about 1°C higher than at the edge. (It is worth pointing out that, to the extent that the surface has a higher in-plane thermal diffusivity than the interior, the internal temperature heterogeneity may be greater than what is observed here.) In order to interpret and predict such non-uniformities, future work will focus on obtaining local internal heat transport/thermal diffusivity constants as functions of the SOC. For example, a thermally isolated cell could be discharged rapidly to a given local SOC creating initial internal temperature gradients. By monitoring local relaxation in the 2D temperature map with time, as the cell rests, it will be possible to derive local internal in-plane heat transport/thermal diffusivity constants at that SOC. And by averaging the temperature over the entire cell as a function of time after a rapid charge/discharge, we can measure local heat transfer coefficients to the environment. Measurements of these constants could enable more quantitative validations of 3D cell models.[1,4,5,40,58]

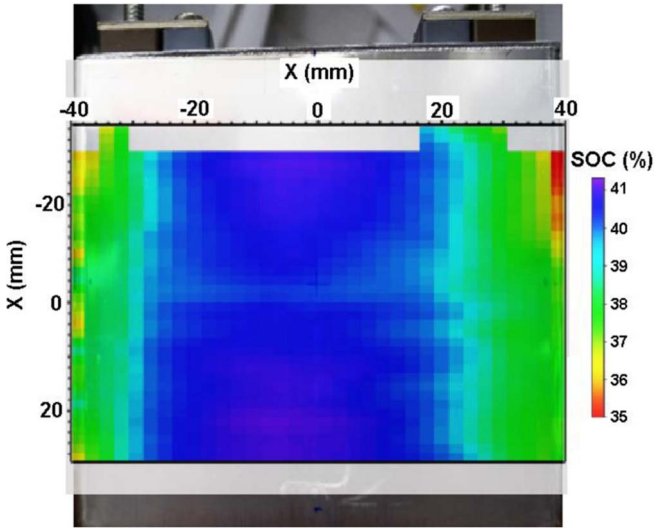

Figure 11. 2D mapping of local SOC in a degraded battery with 60% overall remaining capacity, charged to 4.0V. The location of SOC mapping is illustrated with actual battery in background.

Using the relationship between SOC and the *c* lattice parameter of NMC (Figure 4), we generated an ex-situ 2D SOC map (Figure 11) at the 1785 positions shown in Figure 2 for a battery that had lost 40% of its initial capacity, after about 3,200 high rate cycles at high temperature. While the degradation of the battery in this study is relatively uniform compared to other commercial batteries studied before,[26,27,68] it nevertheless exhibits more severe degradation around the edge than the center, an apparently common pattern. Charged to 4.0 V, the center region of the battery had an SOC of approximately 40%, whereas the left and right edges of the battery were charged to only about 36 to 37%.

Line-of-sight averaging.—We have previously used diffraction measurements to provide 2D maps of the SOC of an LMO pouch cell using the spallation neutron source at ORNL.[26,27] While those measurements were also line-of-sight averages, there was no reason to expect that the SOC should vary systematically along the line of sight—that is, from one electrode sheet to the next. The binding strength of the electrodes to their current collectors may also not vary systematically along the line of sight. However, we do expect a systematic increase in temperature as we go toward the central electrode pair in the pouch. We can estimate the temperature on the pouch centerline if we can guess the functional form for the temperature profile through the cell. In principle, this analysis, performed at every (*x,y*) location, could provide a full 3D temperature map. In the future, we will directly measure the line-of-sight average temperature profile through the thickness of the cell by having the X-ray beam incident on the edge of the cell instead of on its face. The technique of Paxton et al.[28] can also be used to provide information in the third dimension. The use of 3D thermal models will be required to interpret much of this data.

Failure mechanisms.—In addition to indicating where degradation has taken place, our technique can also shed light on local degradation mechanisms, especially in cases where diffraction patterns from both electrodes and both current collectors are available, as in our previous work.[27] This might be accomplished by comparing SOC swings in the electrodes. For example, degradation in the graphite electrode would be indicated if we see LiC_6 while the cathode is still substantially lithiated. Similarly, degradation in the cathode could be indicated if it is delithiated even while the graphite electrode is at LiC_{12}. In cases where active Li loss (to SEI or other parasitic reactions) has occurred, we might see a reduction in the SOC extremes for both electrodes. Finally, we note that this technique could also be useful for cells that have a solid polycrystalline electrolyte, since its XRD spectrum would allow us to detect mechanical strains, and, in the case of a sudden relief of the strain, to detect fractures.

Conclusions

In this paper we describe how we used HE-XRD from the Advanced Photon Source at Argonne to make simultaneous operando line-of-sight non-contact measurements of local SOC, local temperature, and local mechanical strain of the current collectors inside an unmodified commercial (14mm thick) pouch cell. The temperature rise is measured from the expansion of the Cu current collector after removal of mechanically-induced strain. We also suggest how the peak centerline temperature might be estimated to provide 3D temperature maps. We believe that the mechanical strain in the copper current collector is due largely to load transfer from the negative electrode as it lithiates and delithiates. Several local degradation mechanisms—loss of active Li, loss of active anode or cathode material, and debonding of an electrode from its current collector[55,56]—can be identified.

Although all of the operando data described here comes from a single location in the pouch (the center), we are extending our approach to make 2D SOC-dependent operando maps of the temperature, strain, and SOC in fresh and degraded cells. Such maps can be used to measure local thermal diffusivity and heat transfer coefficients within the cell and to the environment as a function of location, temperature and SOC. The spatial resolution of maps such as that shown in Figure 11 is limited only by the beam diameter (0.3 mm here), by the amount of time available to take the data and to carry out the analysis, and by what makes physical sense. We note that for this work each point was interrogated for only on the order of 1 second, so greatly improved signal-to-noise ratios are feasible with longer averaging times.

Acknowledgments

This manuscript has been authored by UT-Battelle, LLC under Contract No. DE-AC05-00OR22725 with the U.S. Department of Energy. Research sponsored by the Clean Vehicles Consortium - US-China Clean Energy Research Center. SJH acknowledges support from the Assistant Secretary for Energy Efficiency, Vehicle Technologies Office of the U.S. Department of Energy (U.S. DOE) under the Advanced Battery Materials Research (BMR) Program. The use of the Advanced Photon Source of Argonne National Laboratory was supported by the U.S. Department of Energy, Office of Science, Office of Basic Energy Sciences. We thank Charles Kurtz for help with the experimental setup.

ORCID

Zhili Feng https://orcid.org/0000-0001-6573-7933

References

1. K. Smith, A. Saxon, M. Keyser, B. Lundstrom, Z. Cao, and A. Roc, "Life Prediction Model for Grid-Connected Li-ion Battery Energy Storage System." In *American Control Conference*, Seattle, WA, 2017.
2. S. Abada, G. Marlair, A. Lecocq, M. Petit, V. Sauvant-Moynot, and F. Huet, "Safety focused modeling of lithium-ion batteries: A review." *Journal of Power Sources*, **306**, 178 (2016).
3. S. J. Harris, A. Timmons, and W. J. Pitz, "A combustion chemistry analysis of carbonate solvents used in Li-ion batteries." *Journal of Power Sources*, **193**(2), 855 (2009).
4. A. Pesaran, "Battery Thermal Management in EVs and HEVs: Issues and Solutions." In *Advanced Automotive Battery Conference*, Las Vegas, NV, 2001.
5. L. Fan, J. M. Khodadadi, and A. A. Pesaran, "A parametric study on thermal management of an air-cooled lithium-ion battery module for plug-in hybrid electric vehicles." *Journal of Power Sources*, **238**, 301 (2013).
6. C. Veth, D. Dragicevic, and C. Merten, "Thermal characterizations of a large-format lithium ion cell focused on high current discharges." *Journal of Power Sources*, **267**, 760 (2014).
7. J. B. Robinson, J. A. Darr, D. S. Eastwood, G. Hinds, P. D. Lee, P. R. Shearing, O. O. Taiwo, and D. J. L. Brett, "Non-uniform temperature distribution in Li-ion

batteries during discharge – A combined thermal imaging, X-ray micro-tomography and electrochemical impedance approach." *Journal of Power Sources*, **252**, 51 (2014).
8. M. Klein, S. Tong, and J. Park, "In-plane nonuniform temperature effects on the performance of a large-format lithium-ion pouch cell." *Applied Energy*, **165**, 639 (2016).
9. A. Samba, N. Omar, H. Gualous, Y. Firouz, P. Van den Bossche, J. Van Mierlo, and T. I. Boubekeur, "Development of an advanced two-dimensional thermal model for large size lithium-ion pouch cells." *Electrochimica Acta*, **117**, 246 (2014).
10. P. Haussmann and J. Melbert, "Internal Cell Temperature Measurement and Thermal Modeling of Lithium Ion Cells for Automotive Applications by Means of Electrochemical Impedance Spectroscopy." *SAE International Journal of Alternative Powertrains*, **6**(2), (2017).
11. A. Raghavan, P. Kiesel, L. W. Sommer, J. Schwartz, A. Lochbaum, A. Hegyi, A. Schuh, K. Arakaki, B. Saha, A. Ganguli, K. H. Kim, C. Kim, H. J. Hah, S. Kim, G.-O. Hwang, G.-C. Chung, B. Choi, and M. Alamgir, "Embedded fiber-optic sensing for accurate internal monitoring of cell state in advanced battery management systems part 1: Cell embedding method and performance." *Journal of Power Sources*, **341**, 466 (2017).
12. G. Zhang, S. Ge, Y. Leng, X. Yang, D. Marple, and C.-Y. Wang, In *Robust Internal Temperature Sensing of Large-Format Li-Ion Cells.pdf>*, Electrochemical Society, 2017.
13. T. Waldmann and M. Wohlfahrt-Mehrens, "In-Operando Measurement of Temperature Gradients in Cylindrical Lithium-Ion Cells during High-Current Discharge." *ECS Electrochemistry Letters*, **4**, 1 (2014).
14. P. J. Osswald, S. V. Erhard, J. Wilhelm, H. E. Hoster, and A. Jossen, "Simulation and Measurement of Local Potentials of Modified Commercial Cylindrical Cells I. Cell Preparation and Measurements." *Journal of The Electrochemical Society*, **162**(10), A2099 (2015).
15. J. P. Schmidt, S. Arnold, A. Loges, D. Werner, T. Wetzel, and E. Ivers-Tiffée, "Measurement of the internal cell temperature via impedance: Evaluation and application of a new method." *Journal of Power Sources*, **243**, 110 (2013).
16. Y. Xiao, "Model-based virtual thermal sensors for lithium-ion battery in EV applications." *IEEE Transactions on Industrial Electronics*, **62**(5), 3112 (2015).
17. C. Forgez, D. V. Do, G. Friedrich, M. Morcrette, and C. Delacourt, "Thermal modeling of a cylindrical $LiFePO_4$/graphite lithium-ion battery." *Journal of Power Sources*, **195**(9), 2961 (2010).
18. Y. Tripathy, A. McGordon, J. Low, and J. Marco, "Internal temperature prediction of Lithium-ion cell using differential voltage technique.," 464 (2017).
19. Y. Inui, Y. Kobayashi, Y. Watanabe, Y. Watase, and Y. Kitamura, "Simulation of temperature distribution in cylindrical and prismatic lithium ion secondary batteries." *Energy Conversion and Management*, **48**(7), 2103 (2007).
20. T. Hatchard, D. MacNeil, A. Basu, and J. Dahn, "Thermal model of cylindrical and prismatic lithium-ion cells." *Journal of The Electrochemical Society*, **148**(7), A755 (2001).
21. Q. Wang, P. Ping, X. Zhao, G. Chu, J. Sun, and C. Chen, "Thermal runaway caused fire and explosion of lithium ion battery." *Journal of power sources*, **208**, 210 (2012).
22. V. Srinivasan and C. Wang, "Analysis of electrochemical and thermal behavior of Li-ion cells." *Journal of The Electrochemical Society*, **150**(1), A98 (2003).
23. N. Damay, C. Forgez, G. Friedrich, and M.-P. Bichat, "Heterogeneous behavior modeling of a $LiFePO_4$-graphite cell using an equivalent electrical circuit." *Journal of Energy Storage*, **12**, 167 (2017).
24. S. J. Harris and P. Lu, "Effects of Inhomogeneities—Nanoscale to Mesoscale—on the Durability of Li-Ion Batteries." *The Journal of Physical Chemistry C*, **117**(13), 6481 (2013).
25. S. Müller, J. Eller, C. Burns, M. Ebner, J. R. Dahn, and V. Wood, "Quantifying Inhomogeneity of Lithium Ion Battery Electrodes and its Influence on Electrochemical Performance-X-ray tomography data of four commercial lithium ion battery graphite electrodes." *Journal of The Electrochemical Society*, **165**, 339 (2018).
26. X. L. Wang, K. An, L. Cai, Z. Feng, S. E. Nagler, C. Daniel, K. J. Rhodes, A. D. Stoica, H. D. Skorpenske, C. Liang, W. Zhang, J. Kim, Y. Qi, and S. J. Harris, "Visualizing the chemistry and structure dynamics in lithium-ion batteries by in-situ neutron diffraction." *Sci Rep*, **2**, 747 (2012).
27. L. Cai, K. An, Z. Feng, C. Liang, and S. J. Harris, "In-situ observation of inhomogeneous degradation in large format Li-ion cells by neutron diffraction." *Journal of Power Sources*, **236**, 163 (2013).
28. W. A. Paxton, Z. Zhong, and T. Tsakalakos, "Tracking inhomogeneity in high-capacity lithium iron phosphate batteries." *Journal of Power Sources*, **275**, 429 (2015).
29. J. Cannarella and C. B. Arnold, "Stress evolution and capacity fade in constrained lithium-ion pouch cells." *Journal of Power Sources*, **245**, 745 (2014).
30. H. Mendoza, S. A. Roberts, V. E. Brunini, and A. M. Grillet, "Mechanical and Electrochemical Response of a $LiCoO_2$ Cathode Using Reconstructed Microstructures." *Electrochimica Acta*, **190**, 1 (2016).
31. Q. Liu, H. He, Z. F. Li, Y. Liu, Y. Ren, W. Lu, J. Lu, E. A. Stach, and J. Xie, "Rate-dependent, Li-ion insertion/deinsertion behavior of $LiFePO_4$ cathodes in commercial 18650 $LiFePO_4$ cells." *ACS Appl Mater Interfaces*, **6**(5), 3282 (2014).
32. M. Bianchini, F. Fauth, E. Suard, J. B. Leriche, C. Masquelier, and L. Croguennec, "Spinel materials for Li-ion batteries: new insights obtained by operando neutron and synchrotron X-ray diffraction." *Acta Crystallogr B Struct Sci Cryst Eng Mater*, **71**(Pt 6), 688 (2015).
33. O. Dolotko, A. Senyshyn, M. J. Mühlbauer, K. Nikolowski, and H. Ehrenberg, "Understanding structural changes in NMC Li-ion cells by in situ neutron diffraction." *Journal of Power Sources*, **255**, 197 (2014).
34. H. Zhou, K. An, S. Allu, S. Pannala, J. Li, H. Bilhoux, S. K. Martha, and J. Nanda, "Probing Multiscale Transport and Inhomogeneity in a Lithium-Ion Pouch Cell Using In Situ Neutron Methods." *ACS Energy Letters*, **1**, 981 (2016).
35. R. Weber, C. R. Fell, J. R. Dahn, and S. Hy, "Operando X-ray Diffraction Study of Polycrystalline and Single-Crystal $Li_xNi_{0.5}Mn_{0.3}Co_{0.2}O_2$." *Journal of The Electrochemical Society*, **164**, 2992 (2017).
36. O. A. Drozhzhin, V. D. Sumanov, O. M. Karakulina, A. M. Abakumov, J. Hadermann, A. N. Baranov, K. J. Stevenson, and E. V. Antipov, "Switching between solid solution and two-phase regimes in the $Li_{1-x}Fe_{1-y}Mn_yPO_4$ cathode materials during lithium (de) insertion: combined PITT, in situ XRPD and electron diffraction tomography study." *Electrochimica Acta*, **191**, 149 (2016).
37. S. C. Nagpure, R. Dinwiddie, S. S. Babu, G. Rizzoni, B. Bhushan, and T. Frech, "Thermal diffusivity study of aged Li-ion batteries using flash method." *Journal of Power Sources*, **195**(3), 872 (2010).
38. F. Richter, S. Kjelstrup, P. J. S. Vie, and O. S. Burheim, "Thermal conductivity and internal temperature profiles of Li-ion secondary batteries." *Journal of Power Sources*, **359**, 592 (2017).
39. S. J. Bazinski, X. Wang, B. P. Sangeorzan, and L. Guessous, "Measuring and assessing the effective in-plane thermal conductivity of lithium iron phosphate pouch cells." *Energy*, **114**, 1085 (2016).
40. J. Jaguemont, N. Omar, F. Martel, P. Van den Bossche, and J. Van Mierlo, "Streamline three-dimensional thermal model of a lithium titanate pouch cell battery in extreme temperature conditions with module simulation." *Journal of Power Sources*, **367**, 24 (2017).
41. N. Liu, Z. Lu, J. Zhao, M. T. McDowell, H.-W. Lee, W. Zhao, and Y. Cui, "A pomegranate-inspired nanoscale design for large-volume-change lithium battery anodes." *Nature nanotechnology*, **9**(3), 187 (2014).
42. Y. Qi and S. J. Harris, "In Situ Observation of Strains during Lithiation of a Graphite Electrode." *Journal of The Electrochemical Society*, **157**(6), A741 (2010).
43. D. S. Eastwood, V. Yufit, J. Gelb, A. Gu, R. S. Bradley, S. J. Harris, D. J. L. Brett, N. P. Brandon, P. D. Lee, P. J. Withers, and P. R. Shearing, "Lithiation-Induced Dilation Mapping in a Lithium-Ion Battery Electrode by 3D X-Ray Microscopy and Digital Volume Correlation." *Advanced Energy Materials*, **4**(4), 1300506 (2014).
44. N. P. Padture, M. Gell, and E. H. Jordan, "Thermal barrier coatings for gas-turbine engine applications." *Science*, **296**(5566), 280 (2002).
45. D. Shi, X. Xiao, X. Huang, and H. Kia, "Modeling stresses in the separator of a pouch lithium-ion cell." *Journal of Power Sources*, **196**(19), 8129 (2011).
46. S. J. Harris, R. D. Deshpande, Y. Qi, I. Dutta, and Y.-T. Cheng, "Mesopores inside electrode particles can change the Li-ion transport mechanism and diffusion-induced stress." *Journal of Materials Research*, **25**(8), 1433 (2010).
47. Y. N. Zhou, J. L. Yue, E. Hu, H. Li, L. Gu, K. W. Nam, S. M. Bak, X. Yu, J. Liu, J. Bai, E. Dooryhee, Z. W. Fu, and X. Q. Yang, "High-Rate Charging Induced Intermediate Phases and Structural Changes of Layer-Structured Cathode for Lithium-Ion Batteries." *Advanced Energy Materials*, **6**, 1600597 (2016).
48. S. Stewart and R. Ahmed, "Rolling contact fatigue of surface coatings—a review." *Wear*, **253**(11-12), 1132 (2002).
49. D. Chen, D. Kramer, and R. Mönig, "Chemomechanical fatigue of LiMn1. 95Al0. 05O4 electrodes for lithium-ion batteries." *Electrochimica Acta*, **259**, 939 (2018).
50. A. Thesis Timmons, Visible changes in lithium-ion electrodes upon lithium insertion and removal. Dalhousie University, Halifax, Nova Scotia, 2007.
51. A. Louli, J. Li, S. Trussler, C. Fell, and J. R. Dahn, "Volume, Pressure and Thickness Evolution of Li-Ion Pouch Cells with Silicon-Composite Negative Electrodes." *Journal of The Electrochemical Society*, **164**(12), 2689 (2017).
52. S. Lee, "Molecular Dynamics Study of the Separation Behavior at the Interface between PVDF Binder and Copper Current Collector." *Journal of Nanomaterials*, **2016**, 1 (2016).
53. S. Hu, Y. Li, J. Yin, H. Wang, X. Yuan, and Q. Li, "Effect of different binders on electrochemical properties of $LiFePO_4$/C cathode material in lithium ion batteries." *Chemical Engineering Journal*, **237**, 497 (2014).
54. H. Zheng, L. Zhang, G. Liu, X. Song, and V. S. Battaglia, "Correlationship between electrode mechanics and long-term cycling performance for graphite anode in lithium ion cells." *Journal of Power Sources*, **217**, 530 (2012).
55. M. Dubarry and B. Y. Liaw, "Identify capacity fading mechanism in a commercial $LiFePO_4$ cell." *Journal of Power Sources*, **194**(1), 541 (2009).
56. D. Anseán, M. Dubarry, A. Devie, B. Liaw, V. García, J. Viera, and M. González, "Fast charging technique for high power LiFePO 4 batteries: A mechanistic analysis of aging." *Journal of Power Sources*, **321**, 201 (2016).
57. M. Doyle, T. Fuller, and J. Newman, "Modeling of Galvanostatic Charge and Discharge of the Lithium/Polymer/Insertion Cell." *Journal of The Electrochemical Society*, **140**, 1526 (1993).
58. R. Thiedmann, O. Stenzel, A. Spettl, P. R. Shearing, S. J. Harris, N. P. Brandon, and V. Schmidt, "Stochastic simulation model for the 3D morphology of composite materials in Li–ion batteries." *Computational Materials Science*, **50**(12), 3365 (2011).
59. P. Lu, C. Li, E. W. Schneider, and S. J. Harris, "Chemistry, Impedance, and Morphology Evolution in Solid Electrolyte Interphase Films during Formation in Lithium Ion Batteries." *The Journal of Physical Chemistry C*, **118**(2), 896 (2014).
60. S. J. Harris, A. Timmons, D. R. Baker, and C. Monroe, "Direct in situ measurements of Li transport in Li-ion battery negative electrodes." *Chemical Physics Letters*, **485**(4-6), 265 (2010).
61. S. J. Harris, E. K. Rahani, and V. B. Shenoy, "Direct In Situ Observation and Numerical Simulations of Non-Shrinking-Core Behavior in an MCMB Graphite Composite Electrode." *Journal of The Electrochemical Society*, **159**, 1501 (2012).

62. D.-W. Chung, P. R. Shearing, N. P. Brandon, S. J. Harris, and R. E. Garcia, "Particle Size Polydispersity in Li-Ion Batteries." *Journal of The Electrochemical Society*, **161**, 422 (2014).
63. D. Kehrwald, P. R. Shearing, N. P. Brandon, P. K. Sinha, and S. J. Harris, "Local Tortuosity Inhomogeneities in a Lithium Battery Composite Electrode." *Journal of The Electrochemical Society*, **158**, 1393 (2011).
64. M. Ebner, F. Marone, M. Stampanoni, and V. Wood, "Visualization and quantification of electrochemical and mechanical degradation in Li ion batteries." *Science*, **342**(6159), 716 (2013).
65. S. J. Harris, D. J. Harris, and C. Li, "Failure statistics for commercial lithium ion batteries: A study of 24 pouch cells." *Journal of Power Sources*, **342**, 589 (2017).
66. T. Baumhöfer, M. Brühl, S. Rothgang, and D. U. Sauer, "Production caused variation in capacity aging trend and correlation to initial cell performance." *Journal of Power Sources*, **247**, 332 (2014).
67. S. F. Schuster, M. J. Brand, P. Berg, M. Gleissenberger, and A. Jossen, "Lithium-ion cell-to-cell variation during battery electric vehicle operation." *Journal of Power Sources*, **297**, 242 (2015).
68. M. Klett, R. Eriksson, J. Groot, P. Svens, K. C. Högström, R. W. Lindström, H. Berg, T. Gustafson, G. Lindbergh, and K. Edström, "Non-uniform aging of cycled commercial $LiFePO_4$//graphite cylindrical cells revealed by post-mortem analysis." *Journal of Power Sources*, **257**, 126 (2014).